Quantum synchronization in quadratically coupled quantum van der Pol oscillators

Nissi Thomas and M. Senthilvelan*

Department of Nonlinear Dynamics, School of Physics, Bharathidasan University, Tiruchirappalli, 620024 Tamil Nadu, India



(Received 17 March 2022; accepted 1 July 2022; published 18 July 2022)

We implement nonlinear anharmonic interaction in the coupled van der Pol oscillators to investigate the quantum synchronization behavior of the systems. We study the quantum synchronization in two oscillator models, coupled quantum van der Pol oscillators and anharmonic self-oscillators. We demonstrate that the considered systems exhibit a high-order synchronization through coupling in both classical and quantum domains. We show that, due to the anharmonicity of the nonlinear interaction between the oscillators, the system exhibits phonon blockade in the phase-locking regime, which is a pure nonclassical effect and has not been observed in the classical domain. We also demonstrate that, for coupled anharmonic oscillators, the system shows a multiple resonance phase-locking behavior due to nonlinear interaction. We point out that the synchronization blockade arises due to strong anticorrelation between the oscillators, which leads to phonon antibunching in the same parametric regime. In the anharmonic oscillator case we illustrate the simultaneous occurrence of bunching and antibunching effects as a consequence of simultaneous negative and positive correlation between the anharmonic oscillators. We examine the aforementioned characteristic features in the frequency entrainment of the oscillators using a power spectrum where one can observe normal mode splitting and the Mollow triplet in the strong coupling regime. Finally, we propose a possible experimental realization for the considered system in the trapped ion and optomechanical setting.

DOI: 10.1103/PhysRevA.106.012422

I. INTRODUCTION

Synchronization is the adjustment of rhythms of coupled self-sustained systems around a common frequency, which were once independent systems with different frequencies [1]. It is a ubiquitous phenomenon occurring in different physical, biological, and chemical systems such as neuronal networks, power-grid networks, circadian rhythm in mammmals, electrical circuits, lasers, orbital resonances in planetary systems, and so on. Some noted examples with an interesting application of synchronization are heart cardiac pacemaker cells, chaotic laser signals, and micromechanical oscillators [2–6]. Synchronization is a well-understood phenomenon in classical systems and it was studied in different contexts. For example, self-sustained oscillators with external drive, two coupled systems, and globally coupled systems with random frequencies such as the Kuramoto model [7,8].

Recent developments of quantum systems such as nanome-chanical oscillators [9], superconducting circuits [10,11], quantum electrodynamics [12], and trapped ions [13], have witnessed significant progress. Since these systems exhibit synchronization properties like limit cycle oscillations, nonlinearity, and so on, the idea of synchronization in the quantum regime emerged. With these developments, synchronization effects in different quantum systems such as atomic ensembles [14–16], Josephson circuits [17], stochastic systems [18], Kerr-anharmonic oscillators [19], micromasers [20], and spin systems [21–24] have been studied recently. Synchronization behaviors were also investigated

in experimental platforms such as optomechanical systems [25–33], nanomechanical oscillators [34], and superconducting devices [35] in the quantum domain. These works shed light on several quantum aspects of quantum synchronization where quantum effects play a dominant role in the synchronicity of the systems. Several measures of synchronization were also proposed in these works to analyze the synchronization behavior in the quantum regime [25,36,37].

Van der pol oscillators are self-sustained systems which are simple and excellent models to study synchronization. Recent works characterized different synchronization behaviors in the context of quantum van der Pol oscillator. In these works, different quantum synchronization behaviors such as limit cycle [38], frequency entrainment [39,40], amplitude death phenomena [41], quantized synchronization behavior [19], and the enhancement of synchronizaton through squeezing [42] were investigated. An effective quantum model was also proposed to capture the underdamped phase dynamics, which helped to identify a quality factor for the quantum coherence [43]. In dissipative coupled quantum van der Pol oscillators the existence of entanglement between the coupled oscillators [44], frequency entrainment [40], and amplitude death [41] was investigated. The quantum van der Pol oscillator has its relevance in the trapped ion experiment as well. Quantum synchronization in the context of trapped ions was investigated by the authors of [38]. A trapped ion is an ideal platform for quantum information processing and quantum computations due to their better coherence time and quantum control. The trapped ions experience nonlinear Coulomb interactions between ion modes. The cross-Kerr nonlinear terms arising in the Coulomb interaction can be implemented as a nonlinear interaction between the ion modes, which shifts the normal mode frequency of the ion motion [45].

^{*}Corresponding author: velan@cnld.bdu.ac.in

In this work, we consider such nonlinear Coulomb interaction between two van der Pol oscillators. In nonlinear susceptible materials this kind of interaction is called $\chi^{(2)}$ nonlinearity and is known to exhibit nonclassical effects like phonon or photon blockade and strong anticorrelation between photon or phonons in optical systems [46–50]. Recently, phonon antibunching was investigated in the quantum van der Pol oscillator, which significantly depended on two-phonon loss [51]. Quantum correlations due to entanglement were investigated in the coupled cavities with second-harmonic generation [47]. Motivated by the above, in this work, we investigate the effect of nonlinear interaction in the phase-locking dynamics of two quantum van der Pol oscillators. We also investigate the phase dynamics of anharmonic self-oscillators with this nonlinear interaction. Using perturbation analysis, we obtain expressions for the steady state and also for the synchronization measure, and analyze the system analytically and numerically. Our results show that, due to strong correlations between the oscillators, the synchronization peaks suppress at resonance with increasing coupling strength. Further, strong anticorrelations between the oscillators also lead to antibunching. We demonstrate that the nonlinear interaction between the anharmonic self-oscillators causes the system to exhibit multiple resonances in the phaselocking regime. Further, we show that, in the phase-locking parametric regime, the oscillators are simultaneously correlated and anticorrelated at different resonances and as a result the system exhibits bunching and antibunching effects simultaneously. We show that these synchronization behaviors are purely nonclassical and were not observed in the classical regime. Finally, we illustrate the above characteristics using the power spectrum, where we can observe normal mode splitting and the Mollow triplet in the strong coupling regime.

We organize the paper as follows. In Sec. II, we describe the system with cross-Kerr interactions using the master equation of the van der Pol oscillator. We also describe the coupled self-oscillators and also the coupled anharmonic selfoscillators. In Sec. III, we discuss the steady-state dynamics of the system in the classical regime. In Sec. IV, we illustrate the synchronization dynamics due to the nonlinear coupling in the quantum regime. We analytically obtain the expression for steady states of the master equation as well as the expression for the synchronization measure using perturbation theory in the coupling strength and demonstrate the quantum effects in the phase-locking dynamics in the considered system. We also discuss the phonon statistics of the system in the phase-locking parametric regime. In Sec. V, we discuss these characteristics in frequency entrainment using the power mechanical spectrum. Finally, we summarize our results in Sec. VI.

II. MODEL

We consider a nonlinear anharmonic coupling between two quantum van der Pol oscillators. This nonlinear anharmonic interaction is generated by the nonlinear Coulomb interaction between two normal modes of motion of two cotrapped ions [45]. The master equation governing the time evolution of the density matrix ρ of two nonlinearly coupled quantum

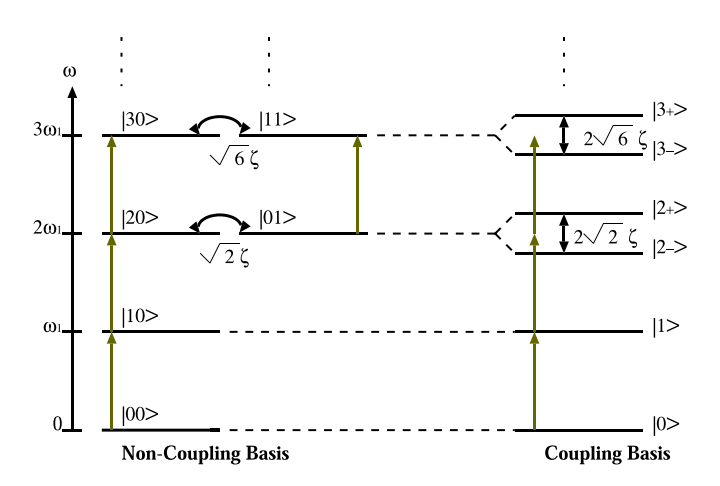


FIG. 1. The schematic energy level diagram of the nonlinearly coupled quantum van der Pol oscillator (without Kerr anharmonicity) in the noncoupling (left) and coupling basis (right).

van der Pol oscillators is described by [38]

$$\dot{\rho} = -i[H_0 + H_I, \rho] + \sum_{i=1}^{2} \gamma_1 \mathcal{L}[a_i^{\dagger}] \rho + \gamma_2 \mathcal{L}[a_i^2] \rho, \quad (1)$$

where $a_i(a_i^{\dagger})$ are the annihilation (creation) operators of the *i*th oscillator. The system Hamiltonian is given by

$$H_0 = \sum_{i=1}^{2} \omega_i a_i^{\dagger} a_i + K_i a_i^{\dagger 2} a_i^2, \tag{2}$$

where ω_i is the natural frequency and K_i is the Kerr strength of the *i*th oscillator. In the absence of Kerr nonlinearity, the system has an energy spectrum as illustrated in Fig. 1 in the noncoupling basis. The presence of Kerr nonlinearity in the system Hamiltonian H_0 brings the anharmonicity in the energy spectrum and this leads to a spacing of $\omega_i + (m+1)K_i$ between the mth and (m + 1)th levels of the energy spectrum of the ith oscillator, which in turn brings a shift in the energy levels of the Fock states [41]. The Lindbland operator $\mathcal{L}[\hat{o}]\rho = \hat{o}\rho o^{\dagger} - \frac{1}{2}\{\hat{o}^{\dagger}\hat{o}\rho + \rho\hat{o}^{\dagger}\hat{o}\}\$ describes the nonunitary dynamics of the system and the parameter γ_1 in (1) denotes the rate of phonon gain and γ_2 is the rate of nonlinear phonon loss. As the nonlinear phonon rate (γ_2) increases the oscillator occupies fewer phonon Fock states. Therefore, in the limit $\gamma_2/\gamma_1 \to \infty$ the system shows a discrete level structure and this corresponds to the quantum limit where the radius of the limit cycle decreases. On the other hand, if the limit $\gamma_2/\gamma_1 \rightarrow$ 0, the radius of the limit cycle increases and the system becomes highly excited. As a result, the system approaches the classical limit. The nonlinear interaction Hamiltonian H_I is considered in the following form:

$$H_I = \zeta \left(a_1^{\dagger 2} a_2 + a_1^2 a_2^{\dagger} \right), \tag{3}$$

with ζ as the coupling strength. The nonlinear interaction H_I mediates the conversion of the phonon of the first oscillator into two phonons of the second oscillator and vice versa and as a result the eigenenergies of the system changes. We study the dynamics of the system (1) using this nonlinear interaction (3) in two oscillator models, namely (i) quantum self-oscillators [K = 0 in (2)] and (ii) anharmonic self-oscillators $[K \neq 0 \text{ self-oscillators}]$

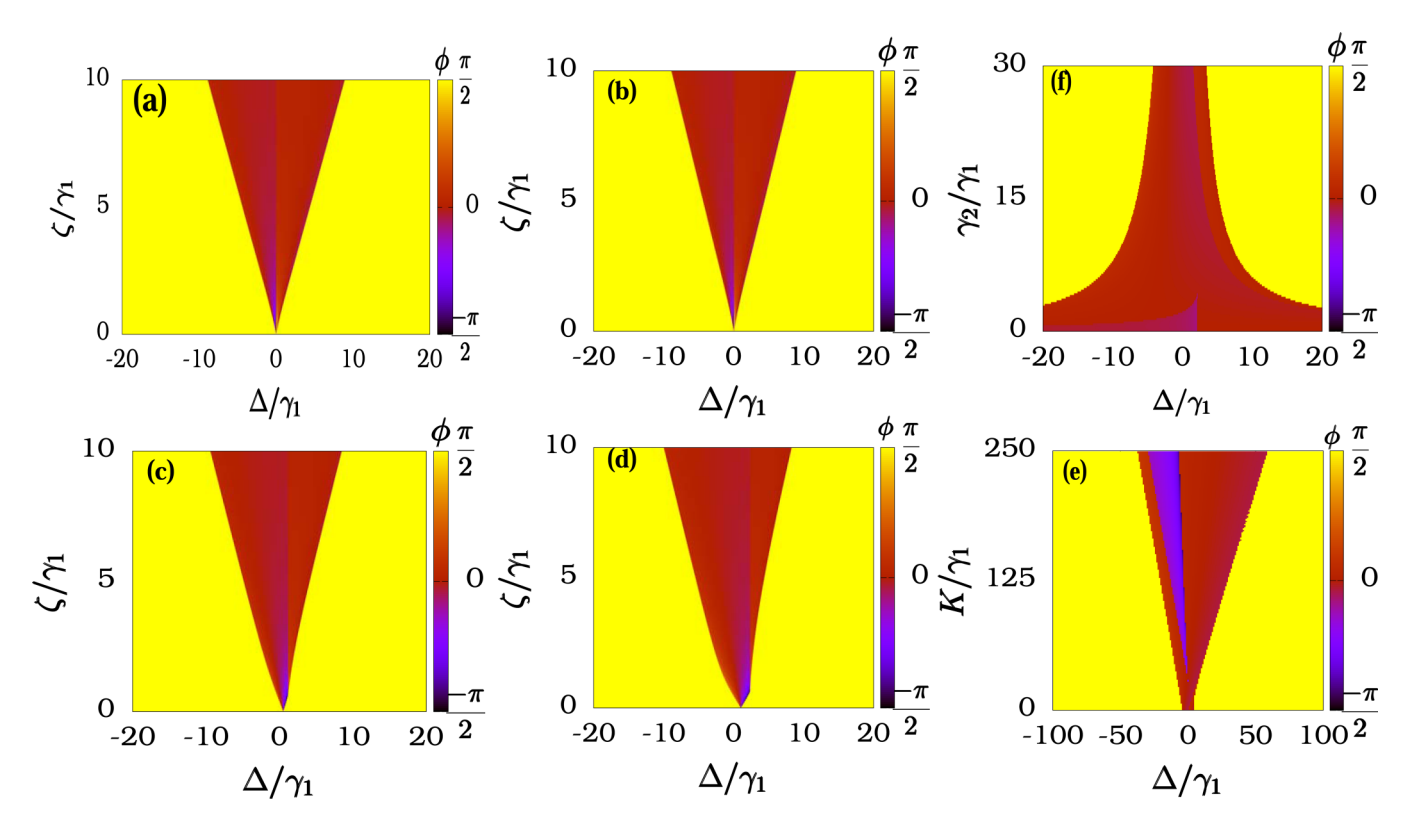


FIG. 2. Phase-locking behavior of steady states in classical regime. Synchronization regime plotted as a function ζ and Δ for (a) $K=0\gamma_1$, (b) $K=0.1\gamma_1$, (c) $K=5\gamma_1$, and (d) $K=10\gamma_1$ with $\gamma_2/\gamma_1=10$. Panel (e) illustrates the phase-locking behavior of the steady state as a function of K and Δ with $\zeta=5$ and $\gamma_2/\gamma_1=10$. Panel (f) shows the phase-locking behavior as a function of γ_2/γ_1 and Δ with K=10 and K=10

in (2)]. We illustrate the energy spectrum of the Hamiltonian $H_0 + H_I$ with K = 0 in Fig. 1. In the noncoupling basis $|n_1, n_2\rangle$ represents the Fock states of the coupled system, where $|n_1\rangle$ and $|n_2\rangle$ correspond to Fock states of the first and second oscillator, respectively. In Fig. 1, |00\rangle represents the ground state and |10\range represents the first excited state. In the absence of the coupling ($\zeta = 0$) the bare energy eigenstates $|20\rangle$ and $|01\rangle$ and the energy eigenstates $|30\rangle$ and $|11\rangle$ are degenerate in the second excitation manifold (n = 2) and third excitation manifold (n = 3), respectively. In the coupling basis $|0\rangle = |00\rangle$ and $|1\rangle = |10\rangle$ represents the ground and first excited states. In the second excitation manifold (n = 2) the coupling lifts the degeneracy of the eigenstates $|20\rangle$ and $|01\rangle$ and these eigenstates split into two nondegenerate states $|2_{\pm}\rangle=\frac{1}{\sqrt{2}}(|20\rangle\pm|01\rangle)$ with a separation of $2\sqrt{2}\zeta$. Similarly, in the third excitation manifold (n=3) the degeneracy between the states |30\rangle and |11\rangle is lifted off, giving rise to two nondegenerate states $|3_{\pm}\rangle = \frac{1}{\sqrt{2}}(|30\rangle \pm |11\rangle)$ with a separation of $2\sqrt{6}\zeta$. In the following, we analyze the phase-locking behavior in the classical and quantum domains of the coupled systems with K = 0 and $K \neq 0$ in (2) and point out the features that exist only in the quantum regime.

III. SYNCHRONIZATION IN CLASSICAL REGIME

First we consider the system (1) in the limit $\gamma_2/\gamma_1 \to 0$ where the limit cycle amplitude of the system becomes large. Applying the Heisenberg equation of motion followed by

the mean-field approximation, the equations of motion for the limit cycle amplitudes $\alpha_1 = \langle a_1 \rangle$ and $\alpha_2 = \langle a_2 \rangle$ can be formulated as

$$\dot{\alpha}_{1} = \left(-i\omega_{1} - 2iK|\alpha_{1}|^{2} + \frac{\gamma_{1}}{2} - \gamma_{2}|\alpha_{1}|^{2}\right)\alpha_{1} - 2i\zeta\alpha_{1}^{*}\alpha_{2},$$

$$\dot{\alpha}_{2} = \left(-i\omega_{2} - 2iK|\alpha_{2}|^{2} + \frac{\gamma_{1}}{2} - \gamma_{2}|\alpha_{2}|^{2}\right)\alpha_{2} - i\zeta\alpha_{1}^{2}.$$
(4)

Using polar coordinates, $\alpha_1 = r_1 \exp(i\theta_1)$ and $\alpha_2 = r_2 \exp(i\theta_2)$, (4) can be rewritten as a phase and amplitude equation in the form

$$\dot{r}_{1} = \left(\frac{\gamma_{1}}{2} - \gamma_{2} r_{1}^{2}\right) r_{1} + 2\zeta r_{1} r_{2} \sin \phi,
\dot{r}_{2} = \left(\frac{\gamma_{1}}{2} - \gamma_{2} r_{2}^{2}\right) r_{2} - \zeta r_{1}^{2} \sin \phi,
\dot{\phi} = -\Delta - 2K \left(r_{2}^{2} - 2r_{1}^{2}\right) - \zeta \left(\frac{r_{1}^{2} - 4r_{2}^{2}}{r_{2}}\right) \cos \phi, \tag{5}$$

where $\phi = \theta_2 - 2\theta_1$ is the phase difference and $\Delta = \omega_2 - 2\omega_1$ is the frequency detuning. From (5) we can say that the system (4) is synchronized when the frequency of the second oscillator becomes twice the frequency of first oscillator $(\omega_2 = 2\omega_1)$, and a fixed relative phase relation is established between them. Therefore, in the rotating frame, finding the stable fixed point can determine the synchronized regime of the system. In Fig. 2 the synchronized regime (dark colored region showing the Arnold tongue) is illustrated which corresponds to a stable fixed point of (4) and we plotted the relative phase ϕ as the color scale in Fig. 2.

In the steady-state regime the amplitude and phase of the system are given by the expressions

$$r_1^* = \sqrt{z}r_2^*, \quad r_2^* = \sqrt{\frac{\gamma_1}{2\gamma_2} \frac{(z+2)}{(z^2+2)}},$$

$$\phi^* = \tan^{-1} \left[-\frac{\gamma_2 r_2^{*2}}{\Delta + 2K r_2^{*2} (1-2z)} \frac{(z-1)(z-4)}{(z+2)} \right], \quad (6)$$

where r_1^* , r_2^* , and ϕ^* represent the steady-state amplitudes and phase of the coupled system (4) and the expression of z can be obtained by solving the following quintic polynomial, that is,

$$\frac{\gamma_1}{2\gamma_2}\zeta^2(z+2)(z^2+2)(z-4)^2 - \frac{\gamma_1^2}{4}(z-1)^2(z-4)^2 - \left(2K\frac{\gamma_1}{2\gamma_2}(1-2z)(z+2) + \Delta(z^2+2)\right)^2 = 0.$$
 (7)

Using linear stability analysis, we find that out of five possible roots of z only two are stable and as we increase the value of K one of these stable stationary states becomes unstable. In Fig. 2 we illustrate the region where the nonlinearly coupled system (4) is synchronized corresponding to the stationary states given in (6) and (7) for different values of K. Figure 2(a) shows the synchronization regime (or Arnold tongue) of the coupled system for K = 0. We studied the dynamics of the system (4) for K = 0 in detail very recently [52]. Here we show that the system exhibits high-order synchronization and multistable behavior, which arises due to the presence of rotational symmetry in the system. For $\Delta = 0$ (and K = 0) we obtain steady-state solutions corresponding to $\cos \phi^* = 0$ and $r_1^* = 2r_2^*$ from the phase equation given in (5). For $\cos \phi^* = 0$, there exists two solutions for ϕ^* , that is, $\phi^* = \pi/2$ and $\phi^* =$ $3\pi/2$. Among these two, only the steady state corresponding to $\phi^* = \pi/2$ is stable for $\zeta < \zeta_c$. When we increase the value of the coupling strength, beyond a critical coupling strength $(\zeta > \zeta_c)$, the steady-state solution corresponding to $\phi^* = \pi/2$ loses its stability. One may find that the following two stable solutions for ϕ^* [52],

$$\phi^* = \phi_0 \quad \text{and} \quad \phi^* = -\phi_0 + \pi,$$

$$\phi_0 = \sin^{-1}\left(\frac{1}{2\zeta}\sqrt{\frac{\gamma_1\gamma_2}{6}}\right),$$
(8)

corresponding to $r_1^* = 2r_2^*$ arise from the critical point. For both the values of ϕ^* , since the solutions given in Eq. (8) are stable, the system exhibits a multistable behavior and as a result the system exhibits clockwise and anticlockwise rotations in the same periodic orbit. Therefore, the values of ϕ^* corresponding to lower values of coupling strength $(\pi/2)$ and higher values of coupling strength [given in (8)] determines the synchronization regime for $\Delta = 0$, which is presented in Fig. 2(a). For $\Delta \neq 0$, the phase deviates from the aforementioned values and attains values corresponding to one of the stable stationary states given in (6) (for K = 0) and the Arnold tongue is obtained as shown in Fig. 2(a). For $\Delta \neq 0$ the system exhibits multistability and oscillators move along the clockwise and anticlockwise directions in different periodic orbits. For $K \neq 0$, we demonstrate the synchronization regime of the system (4) in Figs. 2(b) to 2(d). As mentioned earlier, the system exists in two stable stationary states and displays

clockwise and anticlockwise motions in two periodic orbits. As we increase the value of K, one of the stable stationary states becomes unstable. From (6) we can infer that, for lower values of K, the tip of the Arnold tongue coincides with $\Delta=0$ as shown in Fig. 2(b). For higher values of K there is a shift in the tip of the Arnold tongue from $\Delta=0$ as shown in Figs. 2(c) and 2(d). The phase locking also increases with increasing Kerr strength for a range of Δ values as shown in Fig. 2(e). The damping parameter γ_2/γ_1 rescales the synchronization regime as presented in Fig. 2(f), which enters into the steady state through r_1^* and r_2^* .

IV. SYNCHRONIZATION IN QUANTUM REGIME

Now we explore the dynamical features of the system (1) that comes out due to the presence of nonlinear coupling in the quantum limit $(\gamma_2/\gamma_1 \to \infty)$. The phase-locking behavior in the classical regime discussed in Sec. III is also maintained in the quantum regime with stronger phase-locking features [38]. In this section, we demonstrate certain quantum features that exist in the system due to the presence of coupling. To begin, we analytically obtain the steady-state approximation of the master equation (1) using perturbation theory and derive the synchronization measure to gain some analytical understanding about the synchronization behavior in the quantum regime.

A. Perturbation analysis

The steady-state density matrix of the uncoupled oscillators can be factorized as $\rho^{(0)} = \rho_1^{(0)} \otimes \rho_2^{(0)}$, where $\rho_i^{(0)}$ has a diagonal form and is given by the expression

$$\rho_i^{(0)} = \frac{\left[(\gamma_1/\gamma_2)^n \Theta(1+n, \gamma_1/\gamma_2+n, \gamma_1/\gamma_2) \right]}{\left[(\gamma_1/\gamma_2)_n \Theta(1, \gamma_1/\gamma_2, 2\gamma_1/\gamma_2) \right]}, \quad i = 1, 2 \quad (9)$$

where $(\gamma_1/\gamma_2)_n$ denotes the Pochammer symbol and Θ is the Kummer's confluent hypergeometric function [53]. When the oscillators are uncoupled the quantum van der Pol oscillators are said to exhibit limit cycle oscillations both in the absence (K=0) and presence $(K\neq0)$ of Kerr nonlinearity [41]. This is clear from (9) since $\rho_i^{(0)}$ only depends on the parameter γ_1/γ_2 . Therefore, in the limit $\gamma_2/\gamma_1 \to \infty$, $\rho_i^{(0)}$ can be approximated as $\rho_i^{(0)} \to \frac{2}{3}|0\rangle\langle 0| + \frac{1}{3}|1\rangle\langle 1| + \mathcal{O}(1/\gamma_2)$. Now we apply perturbation theory to obtain the steady-state operator of the coupled system. In the weak coupling limit the steady-state operator can be expanded as a power-series expansion in coupling strength ζ in the following form [19], that is,

$$\rho = \rho^{(0)} + \zeta \rho^{(1)} + \cdots, \tag{10}$$

where $\rho^{(0)}$ is given in (9) and $\rho^{(1)}$ is the first-order correction to the density operator. To obtain $\rho^{(1)}$ we decompose the master equation (1) into the perturbation operator $L_I\rho=-i[H_I,\rho]$ and the unperturbed Lindblandian $L_0\rho=\mathcal{L}\rho-i[H_0,\rho]$. Therefore, the first-order correction to the steady-state density operator can be defined as $\rho^{(1)}=-L_0^{-1}L_I\rho$, where L_0^{-1} is the Moore-Penrose pseudoinverse of the unperturbed Liouvillian L_0 [54]. The inverse of the superoperator L_0 can be found by inverting the diagonal elements in the off-diagonal subspace such that $L_0^{-1}|n+2,m-1\rangle\langle n,m|=$

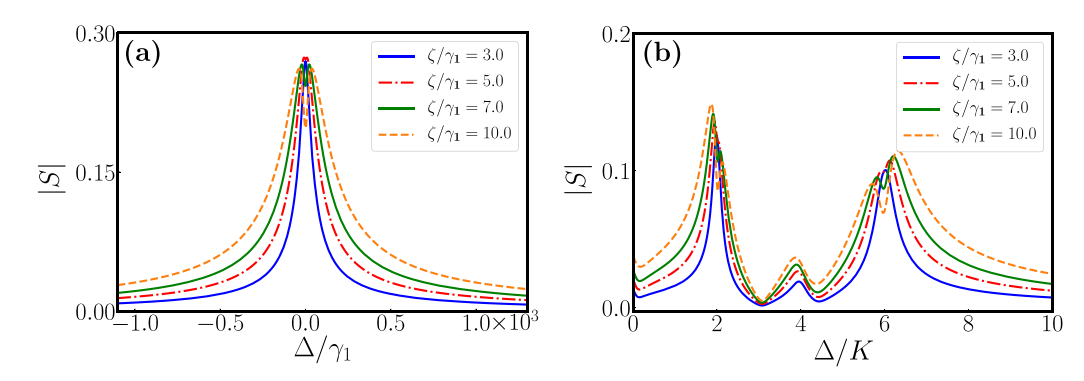


FIG. 3. Synchronization measure |S| for coupled system (1) plotted as a function of frequency detuning Δ with different coupling strengths for (a) K = 0 and (b) $K = 250\gamma_1$ with damping rate $\gamma_2/\gamma_1 = 10$.

$$\lambda^{-1}|n+2,m-1\rangle\langle n,m|$$
 with

$$\lambda = i[\Delta - 2K(2n - m + 2)] - \Gamma, \tag{11}$$

where $\Delta = \omega_2 - 2\omega_1$ is the frequency detuning and $\Gamma = \frac{\gamma_1}{2}[2(n+m)+5] + \gamma_2[(n+2)^2 + (m-1)^2 - 2(n+3)]$. Hence the first-order correction to the density matrix can be obtained in the form

$$\rho_{n+2,m-1;n,m}^{(1)} = \sum_{n=0,m=1}^{\infty} \frac{i\zeta\sqrt{(m)(n+1)(n+2)}\left(\rho_{n,m}^{(0)} - \rho_{n+2,m-1}^{(0)}\right)}{\lambda}.$$
(12)

Since the degeneracy of the eigenstates of the system is lifted up due to the coupling as shown in Fig. 1, it leads to a shift in the eigenstate that can block the transition of phonons for finite detuning in the absence of Kerr nonlinearity (K = 0) and multiple resonances in the presence of Kerr nonlinearity ($K \neq 0$) for the first-order response to the coupling strength. In the following subsection, we will discuss the significance of these two effects in the phase-locking behavior of the system (1).

B. Phase-locking measure

Classically, we identified the relative phase between the oscillators as $\phi = \theta_2 - 2\theta_1$ [(5)]. To quantify the synchronization in the quantum domain, we define the correlator $\langle a_1^{\dagger} a_1^{\dagger} a_2 \rangle$ as the measure of the relative phase between the coupled system, in which $\langle a_j \rangle = |a_j|e^{-i\theta_j}$ (j=1,2) determines the phase of the uncoupled oscillators. Thus, we define the absolute value of the phase synchronization measure in the form [25]

$$S = |S|e^{-i\phi} = \frac{\langle a_1^{\dagger} a_1^{\dagger} a_2 \rangle}{\sqrt{\langle a_1^{\dagger} a_1 \rangle \langle a_2^{\dagger} a_2 \rangle}}$$

$$= \sum_{nm} \frac{\sqrt{m(n+1)(n+2)} \rho_{n+2,m-1}}{\sqrt{\langle a_1^{\dagger} a_1 \rangle \langle a_2^{\dagger} a_2 \rangle}}, \quad (13)$$

where $\phi = \theta_2 - 2\theta_1$ is the relative phase difference between the quantum oscillators. By substituting the expression (12) into (13) we can obtain the synchronization measure for the

first-order correction of density matrix $\rho^{(1)}$ in the form

$$S(\rho^{(1)}) = \sum_{nm} \left(\rho_{nm}^{(0)} - \rho_{n+2m-1}^{(0)} \right) \frac{i\zeta(m(n+1)(n+2))}{\lambda \sqrt{\langle a_1^{\dagger} a_1 \rangle \langle a_2^{\dagger} a_2 \rangle}}, \quad (14)$$

where λ is given in (11).

For K=0, $S(\rho^{(1)})$ given in (14) turns out to be the sum over the terms in (11) at $\Delta=0$ and around $\Delta=\pm 2\sqrt{2}\zeta$ ($\pm 2\sqrt{6}\zeta$ for higher phonon transition) for $\zeta\ll\gamma_2/\gamma_1$ and $\zeta<\gamma_2/\gamma_1$, respectively, of width Γ . For $K\neq 0$, the expression for the synchronization measure is a coherent sum of resonances at $\Delta=2K(2n-m+2)$ and width Γ . In the limit $\gamma_2/\gamma_1\to\infty$, the resonances are more resolved for $K\gg\Gamma$, but as the limit $\gamma_2/\gamma_1\to0$ the resonances are no longer resolved as we can see from Fig. 2(e).

In Fig. 3, we plot the absolute value of synchronization measure S as a function of Δ for different coupling strengths using the steady-state solver of QUTIP [55,56]. In Fig. 3(a) we present the synchronization measure for K = 0. We can observe that, for very weak coupling strength $\zeta \ll \gamma_2/\gamma_1$, the system exhibits resonance peaks at $\Delta = 0$ and as the coupling strength is increased the phase synchronization is suppressed at the resonance $\Delta = 0$ with some finite value such that |S| has a local minima and we observe a split in the synchronization peak around $\Delta = 0$. As we increase the coupling strength, the suppression at the resonance also increases. This can be understood from the energy level diagram given in Fig. 1. For very low values of ζ we observe a $|0\rangle$ to $|1\rangle$ transition with resonant phonon absorption at $\omega_2 = 2\omega_1$ and as a result we obtain single-phase synchronization peaks at $\Delta = 0$. As we increase the coupling strength, the transition from $|1\rangle$ to $|2_{+}\rangle$ gets blocked for detuning $\sqrt{2}\zeta$, hence the synchronization is suppressed at $\Delta = 0$ and we obtain synchronization peaks at $\Delta = \pm 2\sqrt{2}$. Any further increase in the coupling strength ζ also blocks the $|2_{+}\rangle$ to $|3_{+}\rangle$ transition for detuning $(\sqrt{6} - \sqrt{2})\zeta$. This leads to an increase in the suppression of phase synchronization and a split in the synchronization peaks as demonstrated in Fig. 3(a). In Fig. 3(b), we illustrate the phase synchronization measure as a function of Δ for $K \neq 0$. Here we observe that the system exhibits multiple resonances which is clear from (14). The reason for the occurrence of multiple resonances in the presence of Kerr anharmonicity in the energy spectrum of the quantum van der Pol oscillators can be explained by considering the

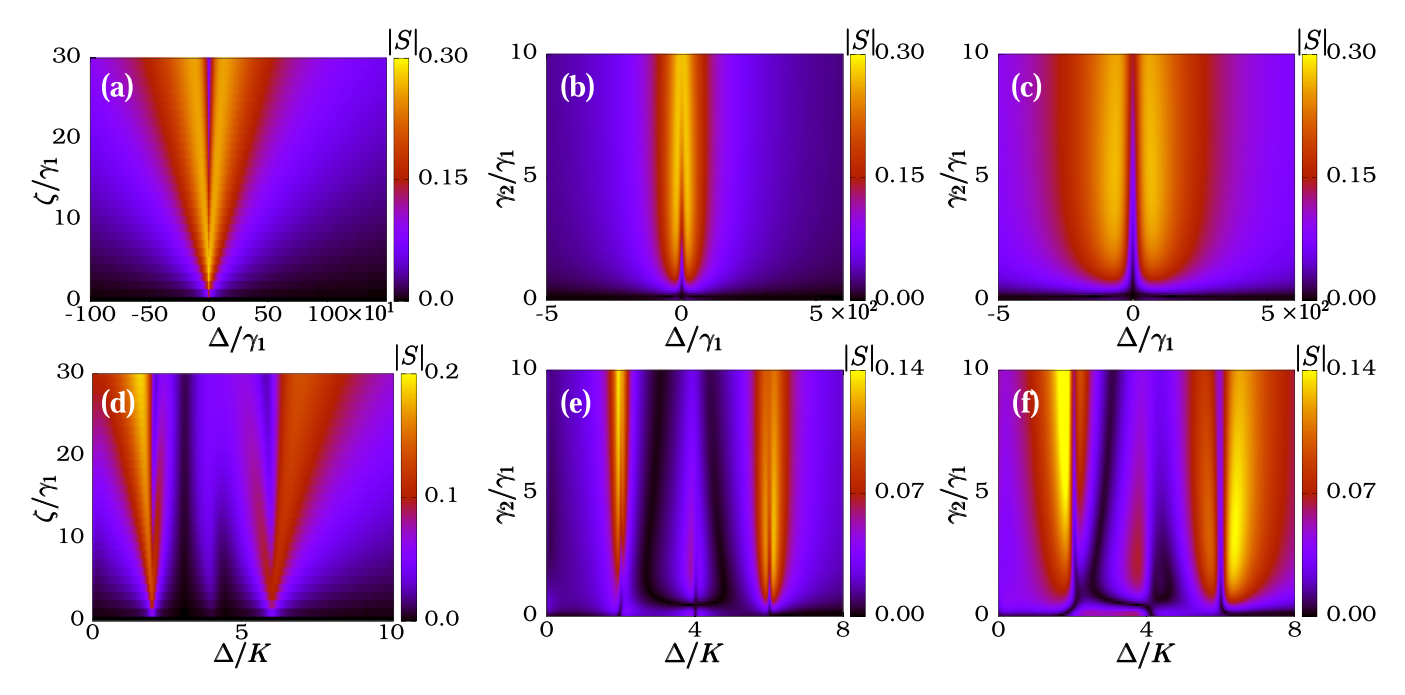


FIG. 4. Different behaviors of the phase-locking measure S for the steady state. Synchronization measure |S| plotted as a function of ζ and Δ in (a) with K=0 and (d) with $K=250\gamma_1$ for $\gamma_2/\gamma_1=10$. The same measure |S| is plotted as a function of γ_2 and Δ with K=0 in (b) for $\zeta=5\gamma_1$, (c) for $\zeta=15\gamma_1$, and with $K=250\gamma_1$ for (e) $\zeta=5\gamma_1$, and (f) $\zeta=15\gamma_1$.

multiple phonon transitions due to the nonlinear interaction term present in (3) where the creation (annihilation) of two phonons is accompanied by the annihilation (creation) of a phonon. This allows a resonant interaction between the states $|n+2,m-1\rangle$ and $|n,m\rangle$ where $|n\rangle$ and $|m\rangle$ are the Fock states of the first and second oscillator. Thus it is required that the energy eigenvalues satisfies the condition $E(|n,m\rangle) = E(|n+2,m-1\rangle)$, which corresponds to $H_0|n,m\rangle = H_0|n+2,m-1\rangle$ such that we obtain a resonance condition of the following form:

$$\Delta + 2K(2n - m) \pm 4K = 0. \tag{15}$$

In [19] the authors obtained a resonance condition which confirmed that coupled identical oscillators (with equal amplitudes) with Kerr anharmonicity in the energy spectrum can show a synchronization blockade and the synchronization can be enhanced by making the oscillators more heterogenous. For the interaction given in (3), classically, we observed that the system exhibits high-order synchronization and for K=0 the synchronization is maximum for the resonance conditions $\omega_2=2\omega_1$ and $r_1^*=2r_2^*$ [52]. For $K\neq 0$ the maximal synchronization occurs for the resonance condition $\omega_2=2\omega_1$ and amplitude ratio $r_1^*:r_2^*=\sqrt{z}:1$ (where z can take the range of parametric values) as given in (6). Therefore, it is clear from the resonance condition (15) that the system is heterogenous and exhibits multiple resonances at $\Delta=2K(2n-m+2)$.

In Figs. 4 and 5, we present an overall picture of the synchronization measure |S| of the steady state (10). Figures 4(a) and 4(d) illustrate the synchronization regimes for K = 0 and $K \neq 0$, respectively. In these two figures, we plot the phase-locking measure |S| as a function of Δ and ζ . Figure 4(a) reveals that, for very low values of ζ , there is no

blockade, and when we increase the coupling strength we can visualize a split in the synchronization tongue at $\Delta = 0$. In Fig. 4(d) we observe the synchronization tongues for $K \neq 0$ and upon increasing the coupling strength, we observe a split in the synchronization tongues at $\Delta = 2K$ and $\Delta = 6K$. We will explain the blockade in more detail in the following subsection. Classically, we observed from Fig. 2 that there is no blockade in the synchronization tongue at $\Delta = 0$ for K=0 and no multiple resonances are present for $K\neq 0$. Figures 4(b) and 4(c) illustrate how the blockade increases for lower values of the damping parameter γ_2/γ_1 at the resonance $\Delta = 0$ and K = 0, as the Fock levels become more populated. For $K \neq 0$, we can also observe the blockade for different Δ values for decreasing γ_2/γ_1 in Figs. 4(e) and 4(f). The resonances are more resolved with the increasing values of K for different coupling strengths, which can be seen from Figs. 5(a) and 5(b). Classically, we observed broadening of the resonance [Fig. 2(e)] for the increasing value of K.

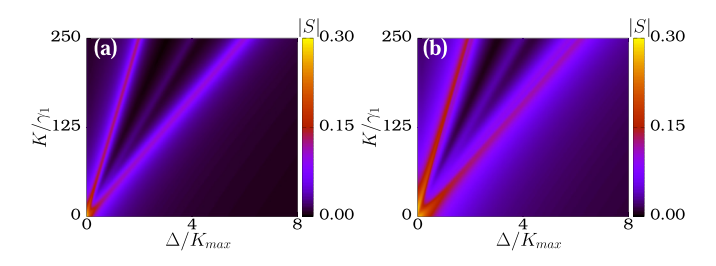


FIG. 5. Absolute value of synchronization measure *S* plotted as a function of frequency detuning Δ and Kerr parameter *K* for the damping rate $\gamma_2/\gamma_1=10$ with coupling strength (a) $\zeta=5.0\gamma_1$ and (b) $\zeta=7.0\gamma_1$ and $K_{\rm max}=250\gamma_1$.

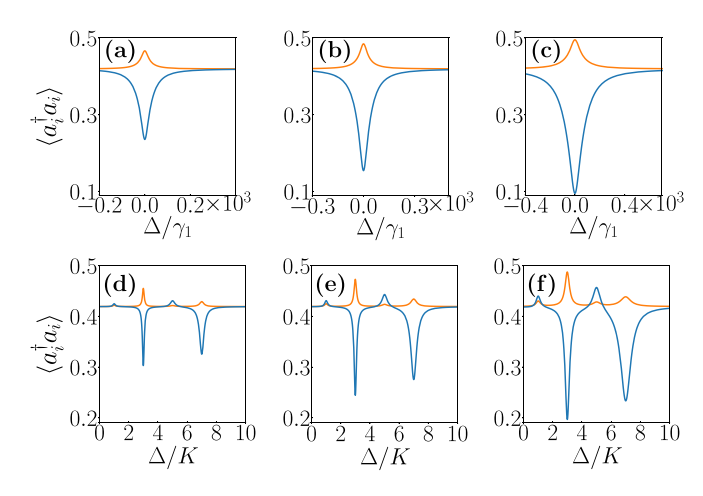


FIG. 6. The phonon number of individual quantum van der Pol oscillators. Here, orange curve represents first oscillator phonon number and blue curve represents second oscillator phonon number. Panels (a)–(c) are plotted for K=0 with (a) $\zeta=3\gamma_1$, (b) $\zeta=5\gamma_1$, and (c) $\zeta=10\gamma_1$. Panels (d)–(f) are plotted for $K=250\gamma_1$ with (d) $\zeta=3\gamma_1$, (e) $\zeta=5\gamma_1$, and (f) $\zeta=10\gamma_1$. In all these figures we consider $\gamma_2=10\gamma_1$.

C. Mutual correlation and antibunching

In the previous subsection we observed a blockade due to the presence of anharmonicity in the energy spectrum due to the nonlinear interaction between two quantum van der Pol oscillators, which is a crucial feature to realize phonon blockade and antibunching in the quantum oscillators. A strong phonon (or photons) correlation between the oscillators causes the system to exhibit limit cycle oscillations such that the system synchronizes with each other, leading to bunching and antibunching [47]. The phonon correlation between two quantum oscillator modes can be calculated using the second-order correlation function [47]

$$g_2(a_1, a_2) = \frac{\langle a_1^{\dagger} a_1 a_2^{\dagger} a_2 \rangle}{\langle a_1^{\dagger} a_1 \rangle \langle a_2^{\dagger} a_2 \rangle},\tag{16}$$

where g_2 is the steady-state second-order correlation function. The two oscillator modes are positively correlated when $g_2 > 1$, leading to simultaneous emission of phonons known as bunching. When $g_2 < 1$ the oscillator modes are negatively correlated and the simultaneous emission of phonons is blocked, known as antibunching. When $g_2 = 1$, there are no correlations between the two oscillator modes. Figure 6 demonstrates the phonon number $\langle a_i^{\dagger} a_i \rangle$ of the first (orange curve) and second (blue curve) oscillator. Figures 6(a) to 6(c) show the phonon correlation between the first and second oscillator for different values of coupling strength ζ for K =0. We can see that the oscillators are anticorrelated with each other and as the coupling strength is increased the oscillators become more negatively correlated. The Wigner dynamics of the first and second oscillator for $\Delta = 0$ is plotted for different coupling strengths in Fig. 7. From Figs. 6(a) to 6(c) we can observe that the phonon number increases very slightly with the increase in coupling strength at $\Delta = 0$, which can be observed in the Wigner function representation in Figs. 7(a), 7(c), and 7(e). We can see that there is no change in the limit cycle of the first oscillator for different

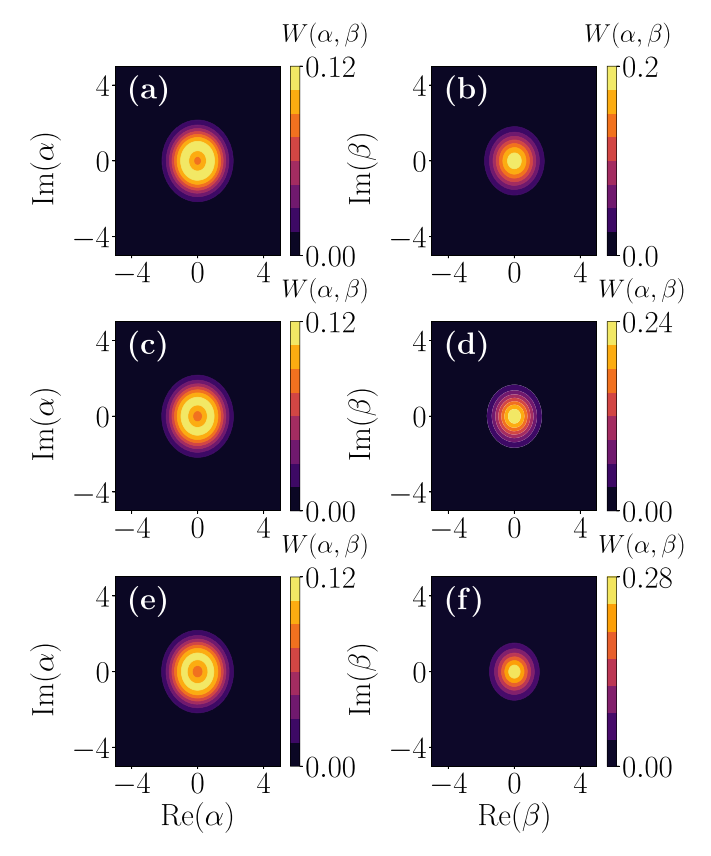


FIG. 7. Wigner distribution function for the steady state of the individual oscillators for K=0. Panels (a), (c), and (e) represent the limit cycle of the first oscillator and panels (b), (d), and (f) represent the limit cycle of the second oscillator. In panels (a), (b) $\zeta=3\gamma_1$, (c), (d) $\zeta=5\gamma_1$, and (e), (f) $\zeta=10\gamma_1$. In all these figures we consider $\gamma_2=10\gamma_1$ and $\Delta=0$.

 ζ values. In Figs. 6(a) to 6(c) a negative increase in the phonon number $\langle a_2^{\dagger} a_2 \rangle$ is observed, which is confirmed from the shrink in the limit cycle as presented in the Wigner distribution function of the second oscillator in Figs. 7(b), 7(d), and 7(f). For $K \neq 0$, the phonon number of the first and second oscillators are plotted in Figs. 6(d) to 6(f). In these figures we can observe the phonon number peaks of the two oscillators at different resonances which are simultaneously correlated and anticorrelated, and this correlation and anticorrelation increases with increasing coupling strength. In Figs. 6(d) to 6(f) we can also observe that the phonon numbers of the first and second oscillators are negatively correlated at $\Delta = 2K$ and $\Delta = 6K$ and positively correlated at $\Delta = 4K$. The Wigner function distribution of the first and second oscillator for different resonance conditions (horizontally) and different coupling strengths (vertically) are plotted in Fig. 8. The limit cycle of the first oscillator remains the same for all values of ζ and Δ , which can be seen from Figs. 8(a), 8(e), and 8(i). The limit cycle of the second oscillator is illustrated in Figs. 8(b) to 8(d) for $\zeta = 3\gamma_1$, Figs. 8(f) to 8(h) for $\zeta = 5\gamma_1$, and Figs. 8(j) to 8(l) for $\zeta = 10\gamma_1$. We can observe that, for anticorrelated phonons, the limit cycle of the second oscillator shrinks as presented in Figs. 8(b), 8(f), and 8(j) for $\Delta = 2K$ and Figs. 8(d), 8(h), and 8(1) for $\Delta = 6K$. For positively correlated phonons the limit cycle of the first and second

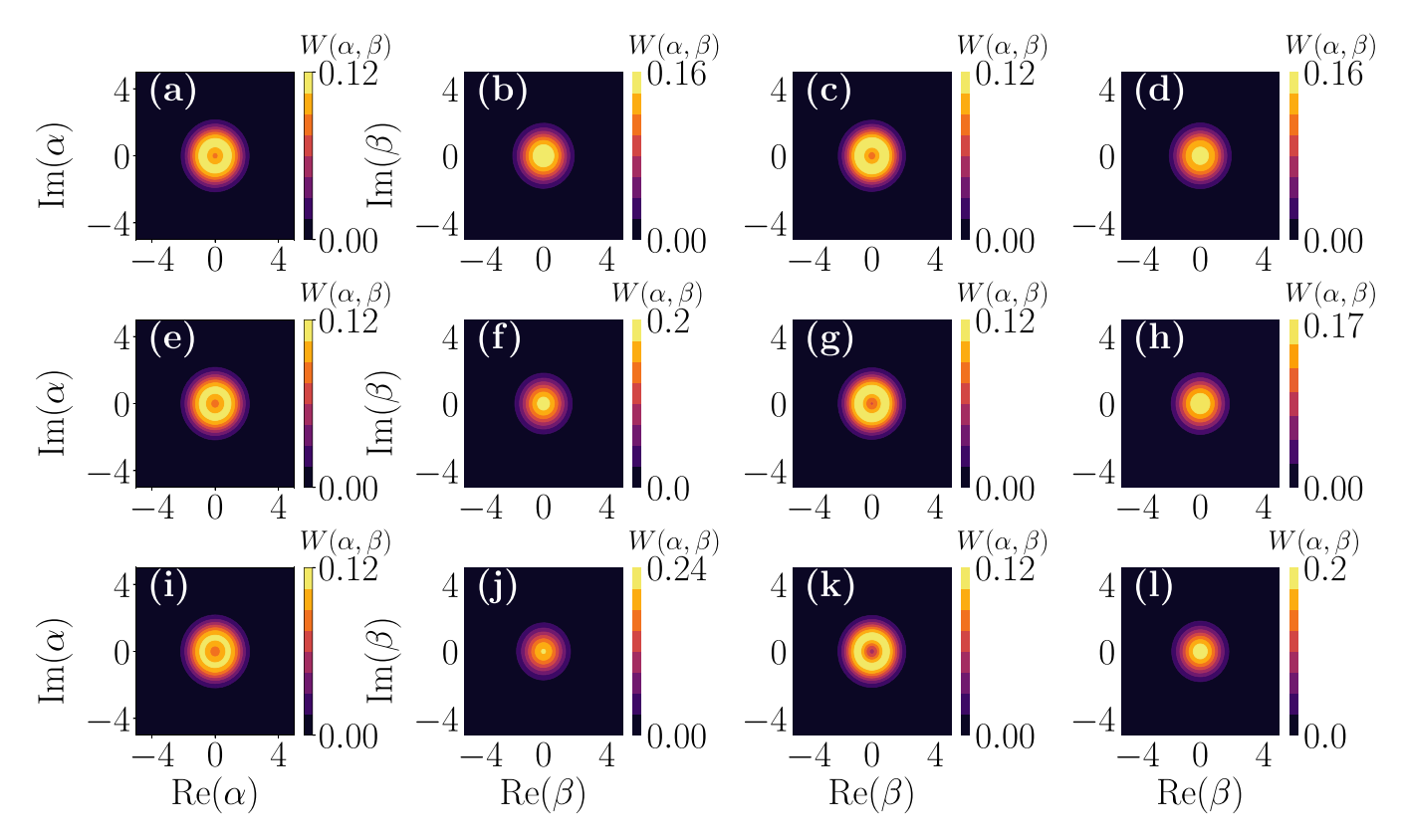


FIG. 8. Wigner distribution function for the steady state of the individual oscillators for $K = 250\gamma_1$ and $\gamma_2 = 10\gamma_1$. Panels (a), (e), and (i) represent the limit cycle of the first oscillator. The limit cycle of the second oscillator is presented in panels (b)–(d) for $\Delta = 2K$, (f)–(h) for $\Delta = 4K$, and (j)–(l) for $\Delta = 6K$. In panels (a)–(d) $\zeta = 3\gamma_1$, (e)–(h) $\zeta = 5\gamma_1$, and (i)–(l) $\zeta = 10\gamma_1$.

oscillators remains the same as shown in Figs. 8(c), 8(g), and 8(k) for $\Delta = 4K$.

With the results now at hand, we analyze the mutual correlation between the quantum van der Pol oscillators through the second-order correlation function given in (16). In Figs. 9(a) and 9(b), we plot the second-order correlation function g_2 as a function of coupling strength for K = 0 and $K \neq 0$, respectively. In Figs. 9(c) and 9(d) we illustrate g_2 as a function of the damping parameter γ_2 , respectively, for K = 0 and $K \neq 0$. For K = 0, we observe that the phonons are anticorrelated, and as such, the second-order correlation function g_2 turns out to be less than 1 for all values of ζ . Hence the system exhibits antibunching, and as we increase the coupling strength, the antibunching also increases as observed from Fig. 9(a). We also notice a split in the antibuching dip, which increases with increasing damping parameter γ_2/γ_1 as shown in Fig. 9(c). For lower values of γ_2/γ_1 we do not observe any split due to resonant absorption during the transition from $|0\rangle$ to $|1\rangle$. Due to this antibunching phenomenon we observe anticorrelation, and as a result, the phonon blockade in the synchronization peaks due to different phonon transitions between the Fock states in the coupling basis is shown in Fig. 1. For $K \neq 0$ we observe simultaneous bunching and antibunching at different resonances as illustrated in Figs. 9(b) and 9(d). At $\Delta = 2K$ and 4K we observe bunching since $g_2 > 1$, which increases with increasing ζ [Fig. 9(b)] and at $\Delta = 6K$ we can see that $g_2 < 1$ and the phonons are antibunched. Because of the presence of this nonclassical effect in the system (1), we observe a synchronization blockade in the quantum regime.

V. POWER SPECTRUM

In the previous section we observed a phonon blockade in the phase-locking regime, and as a consequence of the phonon blockade, we observed antibunching effects in the same parametric region in the coupled quantum van der Pol oscillators. The phonon blockade occurs due to the appreciable excitation-dependent frequency detuning present in the system. In the case of anharmonic quantum van der Pol oscillators, we observed multiple resonance synchronization peaks and simultaneous bunching and antibunching effects at different resonances as a result of anharmonic interaction. We can also investigate these attributes using the power mechanical spectrum defined by [39]

$$P_{ii}(\omega) = \int_{-\infty}^{\infty} dt e^{i\omega t} \langle a_i^{\dagger}(t) a_i(0) \rangle, \quad i = 1, 2, \quad (17)$$

which characterizes the frequency entrainment present in the system. Equation (17) describes the energy spectrum of the oscillators. In Fig. 10 we plot the power spectra $P_{11}(\omega)$ and $P_{22}(\omega)$ against the dimensionless frequency $\tilde{\omega}_i = (\omega - \omega_i)/\gamma_1$ (i=1,2) of the first and second oscillators for different coupling strengths. In Figs. 10(a) and 10(c), for K=0, we observe spectral peaks at $\tilde{\omega}_i = 0$ with $\omega_2 = 2\omega_1$. As we increase the coupling strength, the heights of the spectral peaks decrease and split to form a Mollow triplet in the case of the first oscillator as demonstrated in Fig. 10(a). We observe a normal-mode split in the spectra $[P_{22}(\omega)]$ of the second oscillator when the coupling is strong as shown in Fig. 10.

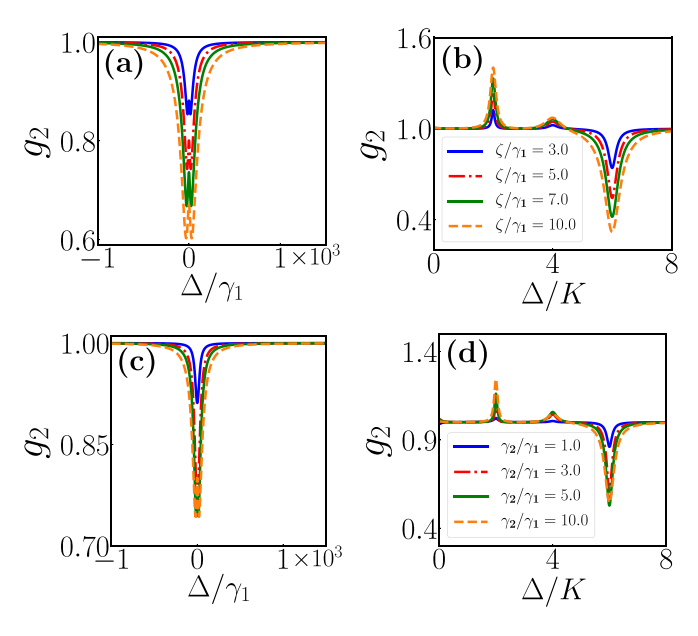


FIG. 9. In panels (a), (b) the correlation function g_2 shown against detuning frequency Δ for different coupling strengths [values of ζ given in the inset of panel (b)] with damping rate $\gamma_2/\gamma_1=10$ and panels (c), (d) for different damping rates [values of γ_2/γ_1 given in the inset of panel (d)] with $\zeta=5.0$ for K=0 in panels (a), (c) and $K=250\gamma_1$ in panels (b), (d).

In the case of the anharmonic oscillator we observe multiple spectral peaks corresponding to the resonance condition given in (15) for increasing frequency ($\tilde{\omega}_i > 0$) for the first and second oscillators as presented, respectively, in Figs. 10(b) and 10(d). Upon increasing the coupling strength we observe

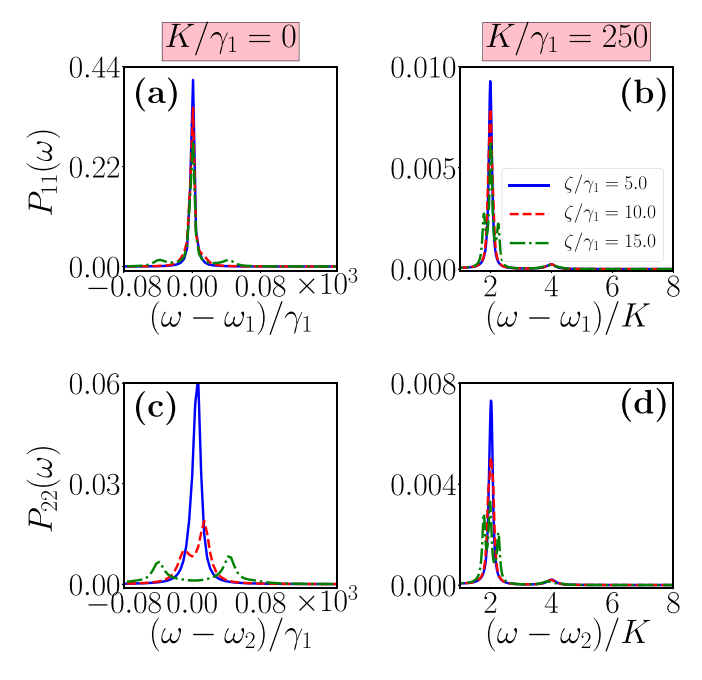


FIG. 10. Power spectra of first oscillator $[P_{11}(\omega)]$ in panels (a) and (b) and second oscillator $[P_{22}(\omega)]$ in panels (c) and (d) shown for different coupling strengths ζ [values given in the inset of panel (b)] for $\gamma_2/\gamma_1 = 10$ and $\Delta = 0$.

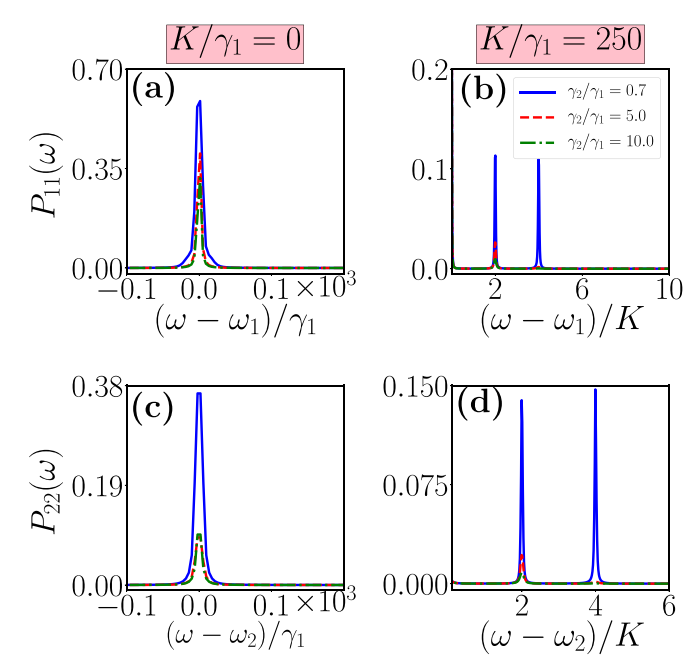


FIG. 11. Power spectra of first oscillator $[P_{11}(\omega)]$ in panels (a) and (b) and second oscillator $[P_{22}(\omega)]$ in panels (c) and (d) shown for different damping parameters γ_2/γ_1 [values given in the inset of panel (b)] for $\zeta = 3.5\gamma_1$ and $\Delta = 0$.

that the Mollow triplet is formed in the spectral peaks of both oscillators at $\tilde{\omega}_i = 0$ and $\tilde{\omega}_i = 2$ as shown in Figs. 10(b) and 10(d). The effect of damping parameters in the spectrum of the oscillators is captured in Fig. 11. By fixing the coupling strength at $\zeta = 3.5\gamma_1$, we illustrate the spectral characteristics for increasing damping parameters for K = 0 and $\Delta = 0$ in Figs. 11(a) and 11(c). For $\gamma_2/\gamma_1 \ll \zeta$, we observe that the Mollow triplet is formed in the spectra of the first oscillator as shown in Fig. 11(a). In the case of the second oscillator, we observe a spectral peak at $\tilde{\omega}_2 = 0$. For $\gamma_2/\gamma_1 > \zeta$, we observe a slight depression in the spectral peak of the second oscillator at $\tilde{\omega}_2 = 0$ as presented in Fig. 11(c). For $\gamma_2/\gamma_1 \gg \zeta$ the height of the spectral peaks gets reduced and we do not observe any strong coupling characteristics. The spectral peaks of anharmonic oscillators for $K \neq 0$ are illustrated in Figs. 11(b) and 11(d). For very low values of the damping parameter we observe the prominent spectral peaks of the first oscillator for different resonance conditions (15) at $\tilde{\omega}_1 = 0$, $\tilde{\omega}_1 = 2$, and $\tilde{\omega}_1 = 4$ as depicted in Fig. 11(b). For the second oscillator the spectral peaks are dominant for $\tilde{\omega_1} = 0$, $\tilde{\omega_1} = 2$ and less prominent for $\tilde{\omega}_1 = 4$. With increasing damping parameters the height of the spectral peaks of the anharmonic oscillators gets suppressed as illustrated in Figs. 11(b) and 11(d).

As discussed previously the transition from the ground state $|0\rangle$ and first excited state $|1\rangle$ is enhanced at resonance $\Delta=0$ for lower values of ζ and there we obtain single spectral peaks for the first and second oscillators for K=0 and multiple spectral peaks for $\tilde{\omega}_i>0$ in the anharmonic case $(K\neq 0)$. As we increase the coupling strength, the transitions between the second and third excited states are far from resonance. Phonon blockade occurs there, and as a result, we observe antibunching effects. The normal mode splitting in the form of the Mollow triplet and two-mode splitting in the

spectral peaks of first and second oscillators, respectively, are the consequences of the aforementioned effects. In the strong coupling regime, the formation of the Mollow-triplet is because of four different allowed transitions ($|3_{+}\rangle \rightarrow |2_{-}\rangle$, $|3_{+}\rangle \rightarrow |2_{+}\rangle$, $|3_{-}\rangle \rightarrow |2_{-}\rangle$, and $|3_{-}\rangle \rightarrow |2_{+}\rangle$) between the second and third excited states and the sideband frequencies occur at $\tilde{\omega}_{i} \pm \omega_{j\pm}$ where $\omega_{j\pm}$ (j=1,2) are the frequencies of the nondegenerate states $|2_{\pm}\rangle$ and $|3_{\pm}\rangle$, respectively. The two-peak normal-mode splitting is due to the blocked transition of the second and third excited states ($|2_{\pm}\rangle$ and $|3_{\pm}\rangle$) with peaks occuring at $\tilde{\omega}_{i} \pm \omega_{j\pm}$. The allowed transition between the Fock states depends on the two-phonon loss rate (γ_{2}/γ_{1}) of the quantum van der Pol oscillators.

Experimental realization

The system represented by (1) can be experimentally achieved via a trapped-ion setup by implementing side-band transitions for two motional modes of frequencies ω_0 and $2\omega_0$, respectively [38]. Then driving the side-band transition of both the modes of resonantly from an excited state we can obtain the coupling described by the Hamiltonian in Eq. (3). The system can be characterized by the Wigner-parity function. The interaction brings out a strong coupling between the modes, which is a desirable property in quantum information processing [45]. Large Kerr nonlinearities can be engineered in trapped ions [19,57,58]. The nonlinearly coupled quantum van der Pol oscillator can also be realized in a cavity optomechanical system [40]. The nonlinear interaction between the mechanical van der Pol oscillators can be realized by quadratically coupling the "membrane-in-the-middle" setup [40,50]. The cavity mode c can be added to the nonlinearly coupled mechanical oscillator and driven with laser at frequency ω_p . The total Hamiltonian is given by

$$H = \omega_0 c^{\dagger} c + E e^{-i\omega_p t} c^{\dagger} + E^* e^{i\omega_p t} c + \sum_{i=1,2} \omega_i a_i^{\dagger} a_i + g_i c^{\dagger} c (a_i + a_i^{\dagger})^2,$$
 (18)

where ω_0 is the cavity frequency, g_i is the optomechanical coupling strength, and E is the driving strength of the laser. Large Kerr anharmonicities are difficult to realize in the optomechanical setup, but can be realized in hybrid systems [41,59,60].

VI. CONCLUSION

In this work we investigated the synchronization dynamics of nonlinearly coupled quantum van der Pol oscillators and those of anharmonic self-oscillators. We showed that the

system exhibits certain novel features in the quantum domain which are not present in the classical domain. We identified that, due to the anharmonicity of the nonlinear coupling, the system exhibits a synchronization blockade in the phaselocking regime. We also showed a quantized phase-locking behavior in nonlinearly coupled anharmonic self-oscillators, which comes out due to the heterogeneity that is present in the system. We illustrated that the phonon blockade in the system, which arises due to anticorrelation between the oscillators, increases with coupling strength. Further, we also demonstrated that, due to the negative correlation between the oscillators, the system shows antibunching effects in the phase-locking parametric regime. In the case of anharmonic self-oscillators, we observed simultaneous correlation and anticorrelation between the oscillators at different resonance peaks, which also leads to simultaneous bunching and antibunching in the system. We identified that the limit cycle of the anticorrelated oscillator shrinks with increasing coupling strength in the Wigner distribution function. We also showed these attributes in the frequency entrainment of the system. The system shows the normal-mode splitting for higher values of the coupling strength, a feature of strong nonlinear interactions. We also observed the Mollow triplet due to multiphonon transitions in the system with increasing coupling strengths.

Phonon and photon blockades in the quantum systems have been an important topic of research since they are a pure quantum effect that leads to antibunching effects in the system. In single-photon detectors, photon correlation is an important tool and has applications in quantum information processing such as quantum teleportation [61–63], quantum cryptography [64,65], and so on. Several theoretical and experimental studies were conducted for the detection of the phonon blockade in optomechanical systems [16,47–50], nanomechanical resonators [66], optical cavity with one trapped atom [67], cavity QED [32], and superconducting microwave resonator [68]. The quantum van der Pol oscillator also provides a feasible phonon source and our studies can help in the realization of phonon detection and quantum information tasks.

ACKNOWLEDGMENTS

N.T. thanks the National Board for Higher Mathematics, Government of India, for providing the Senior Research Fellowship under Grant No. 02011/20/2018 NBHM (R.P)/R&D II/15064 to carry out this work. The work of M.S. forms part of a research project sponsored by the Science and Engineering Research Board, Government of India, under Grant No. CRG/2021/002428.

^[1] A. Pikovsky, M. Rosenblum, and J. Kurths, *Synchronization:* A Universal Concept in Nonlinear Sciences, Cambridge Nonlinear Science Series (Cambridge University Press, Cambridge, England, 2003).

^[2] F. Varela, J. P. Lachaux, E. Rodrigues, and J. Matinerie, Nat. Rev. Neurosci. 2, 229 (2001).

^[3] J. Fell and N. Axmacher, Nat. Rev. Neurosci. 12, 105 (2011).

^[4] A. E. Motter, S. A. Myers, M. Anghel and T. Nishikawa, Nat. Phys. 9, 191 (2013).

^[5] D. Antonio, D. H. Zanette, and D. Lopez, Nat. Commun. 3, 806 (2012).

^[6] S. I. Arroyo and D. H. Zanette, Phys. Rev. E 87, 052910 (2013).

^[7] Y. Kuramoto, Prog. Theor. Phys. Suppl. 79, 223 (1984).

^[8] J. A. Acebrón, L. L. Bonilla, C. J. Perez Vicente, F. Ritort, and R. Spigler, Rev. Mod. Phys. 77, 137 (2005).

^[9] M. Aspelmeyer, T. J. Kippenberg, and F. Marquardt, Rev. Mod. Phys. 86, 1391 (2014).

^[10] J. Clarke and F. K. William, Nature (London) 453, 1031 (2008).

- [11] G. Wendin, Rep. Prog. Phys. 80, 106001 (2017).
- [12] A. Blais, J. Gambetta, A. Wallraff, D. I. Schuster, S. M. Girvin, M. H. Devoret, and R. J. Schoelkopf, Phys. Rev. A 75, 032329 (2007).
- [13] H. Haffner, C. Ross, and R. Blatt, Phys. Rep. 469, 155 (2008).
- [14] B. Zhu, J. Schachenmayer, M. Xu, F. Harrera, J. G. Restrepo, M. J. Holland, and A. M. Rey, New J. Phys. 17, 083063 (2015).
- [15] A. Cabot, G. L. Giorgi, F. Galve, and R. Zambrini, Phys. Rev. Lett. 123, 023604 (2019).
- [16] M. Xu, D. A. Tieri, E. C. Fine, J. K. Thompson, and M. J. Holland, Phys. Rev. Lett. 113, 154101 (2014).
- [17] S. E. Nigg, Phys. Rev. A 97, 013811 (2018).
- [18] I. Goychuk, J. Casado-Pascual, M. Morillo, J. Lehmann, and P. Hänggi, Phys. Rev. Lett. 97, 210601 (2006).
- [19] N. Lörch, E. Amitai, A. Nunnenkamp, and C. Bruder, Phys. Rev. Lett. 117, 073601 (2016).
- [20] D. A. Rodrigues, J. Imbers, and A. D. Armour, Phys. Rev. Lett. 98, 067204 (2007).
- [21] A. Roulet and C. Bruder, Phys. Rev. Lett. 121, 053601 (2018).
- [22] A. Roulet and C. Bruder, Phys. Rev. Lett. 121, 063601 (2018).
- [23] A. W. Laskar, P. Adhikary, S. Mondal, P. Katiyar, S. Vinjanampathy, and S. Ghosh, Phys. Rev. Lett. 125, 013601 (2020).
- [24] J. Tindall, C. Sánchez Muñoz, B. Buča, and D. Jaksch, New J. Phys. 22, 013026 (2020).
- [25] T. Weiss, A. Kronwald, and F. Marquadt, New J. Phys. 18, 013043 (2016).
- [26] E. Amitai, N. Lörch, A. Nunnenkamp, S. Walter, and C. Bruder, Phys. Rev. A 95, 053858 (2017).
- [27] L. Du, C.-H. Fan, H.-X. Zhang, and J.-H. Wu, Sci. Rep. 7, 15834 (2017).
- [28] C.-H. Fan, L. Du, H.-X. Zhang, and J.-H. Wu, J. Phys. B: At. Mol. Opt. Phys. 51, 175503 (2018)
- [29] H. Geng, L. Du, H. D. Liu, and X. X. Yi, J. Phys. Commun. 2, 025032 (2018).
- [30] C.-G. Liao, R. X. Chen, H. Xie, M.-Y. He, and X.-M. Lin, Phys. Rev. A 99, 033818 (2019).
- [31] M. Ludwig and F. Marquardt, Phys. Rev. Lett. 111, 073603 (2013).
- [32] Q. Liao, J. Wen, and W. Deng, Int. J. Theor. Phys. **59**, 1966 (2020).
- [33] G. J. Qiao, X. Y. Liu, H. D. Liu, C. F. Sun, and X. X. Yi, Phys. Rev. A 101, 053813 (2020).
- [34] M. H. Matheny, J. Emenheiser, W. Fon, A. Chapman, A. Salova, M. Rohden, J. Li, M. H. De Badyn, M. Pósfai, L. Duenas-Osario, M. Mesbahi, J. P. Crutchfield, M. C. Cross, R. M. D'Souza, and M. L. Roukes, Science 363, eaav7932 (2019).
- [35] A. M. Hriscu and Y. V. Nazarov, Phys. Rev. Lett. 110, 097002 (2013).
- [36] A. Mari, A. Farace, N. Didier, V. Giovannetti, and R. Fazio, Phys. Rev. Lett. 111, 103605 (2013).
- [37] N. Jaseem, M. Hajdušek, P. Solanki, L.-C. Kwek, R. Fazio, and S. Vinjanampathy, Phys. Rev. Res. 2, 043287 (2020).
- [38] T. E. Lee and H. R. Sadeghpour, Phys. Rev. Lett. 111, 234101 (2013).
- [39] S. Walter, A. Nunnenkamp, and C. Bruder, Phys. Rev. Lett. 112, 094102 (2014).

- [40] S. Walter, A. Nunnenkamp, and C. Bruder, Ann. Phys. (Leipzig) **527**, 131 (2015).
- [41] E. Amitai, M. Koppenhöfer, N. Lörch, and C. Bruder, Phys. Rev. E 97, 052203 (2018).
- [42] S. Sonar, M. Hajdusek, M. Mukherjee, R. Fazio, V. Vedral, S. Vinjanampathy, and L.-C. Kwek, Phys. Rev. Lett. 120, 163601 (2018).
- [43] T. Weiss, S. Walter, and F. Marquardt, Phys. Rev. A 95, 041802(R) (2017).
- [44] T. E. Lee, C.-K. Chan, and S. Wang, Phys. Rev. E **89**, 022913 (2014).
- [45] S. Ding, G. Maslennikov, R. Hablutzel, H. Loh, and D. Matsukevich, Phys. Rev. Lett. 119, 150404 (2017).
- [46] X. W. Xu, H. Q. Shi, A. X. Chen, and Y. X. Liu, Phys. Rev. A 98, 013821 (2018).
- [47] T. E. Lee and M. C. Cross, Phys. Rev. A 88, 013834 (2013).
- [48] Y. H. Zhou, H. Z. Shen, and X. X. Yi, Phys. Rev. A 92, 023838 (2015).
- [49] D. Gerace and V. Savona, Phys. Rev. A 89, 031803(R) (2014).
- [50] H. Xie, C. G. Liao, X. Shang, Z. H. Chen, and X. M. Lin, Phys. Rev. A 98, 023819 (2018).
- [51] J. Li, C. Ding, and Y. Wu, J. Appl. Phys. 128, 234302 (2020).
- [52] N. Thomas, S. Karthiga, and M. Senthilvelan, Eur. Phys. J. Plus 136, 1222 (2021).
- [53] V. V. Dodonov and S. S. Mizrahi, J. Phys. A: Math. Gen. 30, 5657 (1997).
- [54] A. C. Y. Li, F. Petruccione, and J. Koch, Sci. Rep. 4, 4887 (2014).
- [55] J. R. Johansson, P. D. Nation, and F. Nori, Comput. Phys. Commun. 183, 1760 (2012).
- [56] J. Johansson, P. Nation, and F. Nori, Comput. Phys. Commun. 184, 1234 (2013).
- [57] M. Grimm, C. Bruder, and N. Lörch, J. Opt. 18, 094004 (2016).
- [58] J. P. Home, D. Hanneke, J. D. Jost, D. Liebfried, and D. J. Wineland, New J. Phys. 13, 073026 (2011).
- [59] S. Rips, I. Wilson-Rae, and M. J. Hartmann, Phys. Rev. A 89, 013854 (2014).
- [60] A. J. Rimberg, M. P. Blencowe, A. D. Armour, and P. D. Nation, New J. Phys. 16, 055008 (2014).
- [61] D. Boschi, S. Branca, F. DeMartini, L. Hardy, and S. Popescu, Phys. Rev. Lett. 80, 1121 (1998).
- [62] M. Riebe, H. Häffner, C. F. Roos, W. Hänsel, J. Benhelm, G. P. T. Lancaster, T. W. Körber, C. Becher, F. Schmidt-Kaler, D. F. V. James, and R. Blatt, Nature (London) 429, 734 (2004).
- [63] T. Müller, M. Anderson, J. Huwer, J. Skiba-Szymanska, A. B. Krysa, R. M. Stevenson, J. Heffernan, D. A. Ritchie, and A. J. Shields, in *Quantum Information and Measurement* (Optical Society of America, Washington, D.C., 2019), pp. S2A–S24.
- [64] A. K. Ekert, Phys. Rev. Lett. 67, 661 (1991).
- [65] A. Soujaeff, T. Nishioka, T. Hasegawa, S. Takeuchi, T. Tsurumaru, K. Sasaki, and M. Matsui, Opt. Express 15, 726 (2007).
- [66] A. Miranowicz, J. Bajer, N. Lambert, Y. X. Liu, and F. Nori, Phys. Rev. A 93, 013808 (2016).
- [67] K. M. Birnbaum, A. Boca, R. Miller, A. D. Boozer, T. E. Northup, and H. J. Kimble, Nature (London) 436, 87 (2005).
- [68] C. Vaneph, A. Morvan, G. Aiello, M. Féchant, M. Aprili, J. Gabelli, and J. Estéve, Phys. Rev. Lett. 121, 043602 (2018).